Gas Sensing System Based on an All-Fiber Photothermal Microcell

Matej Njegovec, Jure Javornik, Simon Pevec, Vedran Budinski, Tomaz Gregorec, Benjamin Lang, Manuel Tanzer, Alexander Bergmann, and Denis Đonlagić, *Member, IEEE*

***Abstract*—This article presents an all-fiber, miniature Fabry–Perot gas sensor based on photothermal absorption spectroscopy with a custom-made and cost-efficient interrogation system. The sensing gas microcell has a diameter of 125 μm and a length of 1 mm, and allows for free gas exchange within the optical resonator through micromachined slits. High light intensity and confinement are ensured by delivering the excitation light directly into the gas microcell through a lead-in single-mode fiber. This enhances the photothermal effect and provides a short system response time. The interrogation system utilizes the modulation of an excitation laser diode with a fixed frequency while locking the probe laser onto the gas microcell's quadrature point (QP) and observing the variations of the reflected optical power. To show the potential of the proposed system, nitrogen dioxide (NO_2) was measured in dry air. Thereby, a limit of detection of 20 ppm could be achieved for 10 s integration time. Furthermore, the small dimensions of the sensor allow for improved dynamic performance with photothermal modulation frequencies as high as 7 kHz.**

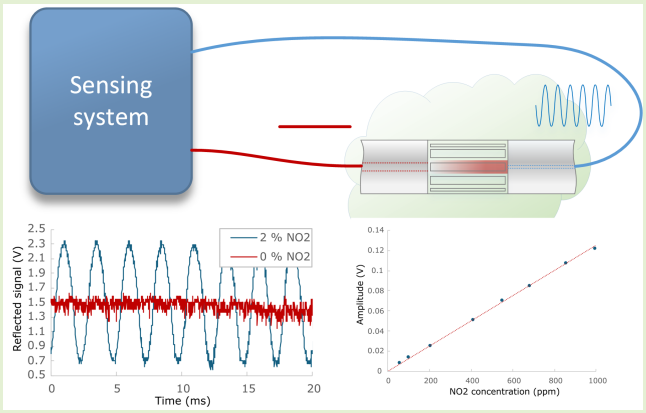

***Index Terms*— Fabry–Perot interferometer (FPI), fiber gas cell, fiber gas sensor, nitrogen dioxide (NO_2), photothermal effect.**

I. Introduction

ON-TIME and online detection of different chemical, biological, radiological, and nuclear (CBRN) events in various environments is crucial to prevent and minimize possible damage to human health and the environment. In this regard, it is very important to selectively monitor concentrations of various hazardous gases and particles that might be present in the environment. Optical gas sensing principles [1], [2] showed high potential due to high selectivity, as most gas molecules have distinctive optical resonant frequencies. Merging bulk optical setups with optical fibers can add further advantages and flexibility to the sensing system, e.g., the possibility for remote sensing (optical fibers allow for transmission over large distances), electric passivity (no electric components within the sensing area), immunity to electromagnetic interference, and compatibility with explosive/hazardous environments. A common part of many optical gas sensing principles is a gas cell, which contains the analyzed gas that is illuminated by excitation light with wavelengths aligned to the absorption peaks of the target species within the analyzed gas. The absorption of light by target species is then identified by using different principles, like gas absorption spectroscopy [3], tunable diode laser absorption spectroscopy (TDLAS) [1], photo-acoustic absorption spectroscopy [4], measurement of the anomalous dispersion of refractive index [2], and many others. While these sensing principles are well established, gas absorption cells remain relatively large (long optical path lengths (OPLs) are required), complex for production (which is associated with increased cost), require relatively large sample volumes, are sensitive to vibrations, temperature, and other environmental impacts, and have limited compatibility with optical fibers. Thus, their applications are limited to a restricted range of operating conditions and cost-tolerant applications.

Photothermal absorption spectroscopy [5] offers the potential for a size reduction of the gas cell. The sample gas is

Manuscript received 22 February 2024; revised 19 April 2024; accepted 22 April 2024. Date of publication 3 May 2024; date of current version 14 June 2024. This work was supported in part by the NATO Science for Peace and Security (SPS) Program under Award SPS G5766 and in part by the Slovenian Research Agency (ARIS) Program under Grant P2-0368. The associate editor coordinating the review of this article and approving it for publication was Dr. Xuehao Hu. *(Corresponding author: Matej Njegovec.)*

Matej Njegovec, Jure Javornik, Simon Pevec, Vedran Budinski, Tomaz Gregorec, and Denis Đonlagić are with the Laboratory of Electro-Optics and Sensor Systems, Institute of Automation, University of Maribor, 2000 Maribor, Slovenia (e-mail: matej.njegovec@um.si; denis.donlagic@um.si).

Benjamin Lang, Manuel Tanzer, and Alexander Bergmann are with the Institute of Electrical Measurement and Sensor Systems, Graz University of Technology, 8010 Graz, Austria (e-mail: benjamin.lang@tugraz.at; alexander.bergmann@tugraz.at).

Digital Object Identifier 10.1109/JSEN.2024.3394651

irradiated periodically using an excitation laser source tuned to an absorption line of the target species. This causes atomic or molecular excitation and subsequent conversion to heat after collisional relaxation. Consequently, variations in the refractive index of the gas are produced within the gas cell, which can be detected using well-known interferometric principles based on Mach-Zehnder [6] or Fabry–Perot [7], [8], [9], [10], [11] interferometers. Periodic excitation of the gas allows the use of phase-sensitive detection techniques [9], [10], which can improve the signal-to-noise ratio (SNR) significantly, and, thus, the sensor's detection limit. Conventional photothermal spectroscopy setups typically utilize free-space optical components to form high-finesse Fabry–Perot interferometers (FPIs) [12]. Free space optical components, like high reflectivity mirrors and collimators, are typically spatially extensive/large (with limited potential for miniaturization) and require precise and environmentally stable alignment to achieve high interferometer finesse. Long-term stability, temperature invariability, and low susceptibility to vibrations [13] thus present a major concern and limitation. The excitation light is applied mostly in a direction perpendicular to the probe laser beam [13], [14], thus decreasing the volume of the heated region significantly [8] (refractive index changes only in a limited volume of the probe beam, i.e., the probe beam is usually focused into a spot along the probe beam, while the usage of the excitation power is weak as the relevant absorption occurs over distances that can not exceed the probe beam diameter). These perpendicular configurations lead to an increase in engineering complexity due to the tight alignment requirements as the probe and excitation beams must intersect [13]. Furthermore, a high-finesse plane parallel Fabry–Perot gas cell requires a collimated probe beam, which often has a large diameter (1–3 mm). This is especially disadvantageous, considering that the photo-thermal signal is indirectly proportional to the diameters of the probe and excitation beam. The excitation beam diameter is also a decisive factor in the dynamic performance of a photo-thermal absorption gas cell, as the cell's time constant depends strongly on the excitation beam's diameter [13].

Various designs of all-fiber photothermal gas sensors were proposed to mitigate these limitations [15]. These designs were based mainly on hollow core/photonic crystal fibers (HC/PCF) [10], [15], [16], [17], [18], [19], [20], which allow for easy alignment and guidance of the excitation and probe beam over longer distances, thus decreasing the detection limits (down to the ppb range). At the same time, high excitation frequencies can be applied (10 [10], 50 [15], 2.7 [16], 12.5 kHz [17], etc.). Nevertheless, the hollow core fiber approach also has significant limitations, like impaired gas exchange among the surrounding and the hollow core gas, which is usually achieved through small side openings [15], leading to long system response times (for example, 40 s in [15], 63 s in [16], 52 s in [18], and 19 s in [19]). Active pumping is often required to introduce gas to a PCF, which compromises its miniaturization potential and electrically passive design. Consequential downsides are their limited suitability for harsh environments and remote operations.

This article proposes a short, all-fiber/all-silica, open path, low-finesse FPI gas microcell design to avoid the above-mentioned limitations. The sensor is based on a gas microcell (Fabry–Perot cavity), that is constructed within an optical fiber (125 μm diameter) and has a length of 1 mm while using collinear excitation with a small (average) radius and probe beams, both delivered through a pair of optical fibers. This assures tight volume overlap of both beams and thus increases variations of a cumulative refractive index along the optical path of the probe beam, which compensates for a lower sensitivity of low finesse FPI. The open and compact design of the gas microcell allows for unobstructed gas exchange, which can significantly improve the response time of the measurement system. The sensor design allows for using the probe and the excitation optical sources that are otherwise not compatible with the standard optical wavelength multiplexers and dual-band fibers (for example, 1550 nm probe and 450 nm excitation wavelengths), increasing its application potential. Established signal processing techniques were applied to extract gas concentration information from the received signal. The operation of the proposed sensor and sensing system is presented for nitrogen dioxide (NO_2) detection.

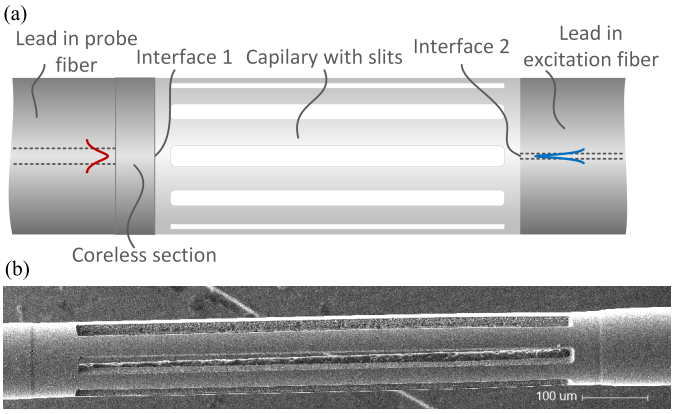

Fig. 1. (a) Sensor design and (b) micromachined sensing structure.

II. Sensor Design, Manufacturing, and Operation

A. Sensor Design

The proposed all-fiber miniature Fabry–Perot sensor design is presented in Fig. 1 and includes an end-capped probe single-mode optical fiber (Corning SMF-28e), suitable for guiding a 1550 nm probe light, a 1 mm long silica capillary with inner and outer diameters of 87 and 125 μm, respectively, and a short-wavelength cut-off single-mode fiber (Corning RGB-400 fiber). The latter is used to deliver the excitation beam to the FP gas microcell. The end-cap surface and the short-wavelength cut-off single-mode fiber define a low-finesse FPI. The end-capping of the SMF-28e fiber with a coreless fiber is required, to maintain a good end surface quality during the production procedure, including splicing and etching steps, as described further below. The thickness of the end cap is approximately 40 μm.

The capillary walls were slitted along the capillary length to allow unobstructed gas exchange into the space between both fiber ends. Six about 35 μm wide slits were formed equidistantly around the capillary tube circumference.

This distribution of slits maintained the circular symmetry of the cell's cross section.

The probe single-mode of 1550 nm was connected to an optical interrogation system, which measured the small variations in the OPL of the FPI, while the excitation (short wavelength range) single-mode fiber was coupled to a moderate power excitation laser diode to provide and deliver excitation light directly into the FPI's active volume.

The presented design allows direct thermo-optic excitation of the gas in a small and confined volume that is well-matched to the probe light volume while maintaining a compact and mechanically rigid design.

B. Sensor Operation and Analysis

The excitation of gas with light at wavelengths corresponding to the target species' absorption band causes temperature variations, which, as a result, changes the refractive index of the gas within the cell. The refractive index change amplitude of the gas due to harmonic laser excitation can be expressed as [21]

$$\widehat{n} = \frac{n-1}{T_0}\frac{\alpha \widehat{P}_{\text{exc}}\tau_T}{\pi a^2 \rho_0 C_p}|E_1\left(i\omega_m \tau_T/2\right)|. \tag{1}$$

Here, T_0 represents the absolute gas temperature, α the gas absorption coefficient at the excitation wavelength, $\widehat{P}_{\text{exc}}$ the excitation optical power amplitude, ρ_0 the gas mixture density, C_p the specific heat of the gas mixture, a the excitation beam diameter, ω_m the modulation angular frequency, $\tau_T = a^2/4D_T$ the characteristic thermal diffusion time constant, D_T the thermal diffusivity of the gas, and $E_1(z)$ represents the exponential integral function. For example, by using 2% NO_2 as a target gas in air ($\alpha_{NO2} = 30$ m^{-1} at 448 nm, $C_p = 1012$ Jkg^{-1}K^{-1}, $\rho_0 = 1.1978$ kg/m^3, $D_T = 2.178 \times 10^{-05}$ m^2/s), in combination with a 448 nm laser source with an excitation power of 70 mW, an excitation frequency f of 400 Hz, and a beam diameter of 100 μm (corresponding to an average mode field radius over the 1 mm in free space), we can expect a variation in the average refractive index of around 4.4×10^{-7} RIU. It is important to note that this estimation neglects the thermal conduction lead in fibers, and also neglects the effects of capillary diameter, walls, and slits on the photothermal effect.

The change of the FPI back-reflected optical power due to variations of the OPL, i.e., the $dP_r/d\text{OPL}$, which determines the system's sensitivity, depends on several factors. The FPI's length (gas cell length) is one of the factors that can be selected optimally to enhance the performance. Since the beams at the output of the probe and excitation fiber are divergent (Fig. 2), the choice of the FPI's length affects the magnitude of the back-reflected probe light and the degree of overlap of the excitation and probe beam volumes.

The optical power reflected from the low finesse FPI can be approximated by a two-beam interference

$$P_r = P_1 + P_2 + 2\sqrt{P_1 P_2}\cos\left(\frac{4\pi \text{OPL}}{\lambda}\right). \tag{2}$$

Herein, λ represents the wavelength of the probe laser, P_1 represents the optical power reflected from the first interface (R_1), while P_2 represents the optical power reflected from the second interface (R_2) after being coupled back into the probe optical fiber. It is important to note that the theoretical model does not include the slitted capillary, which might result in discrepancies between theoretical and practically measured sensitivity. To obtain the change in the reflected optical power due to a change in the interferometer's OPL, (2) is derived as a function of OPL

$$\frac{dP_r}{d\text{OPL}} = -\frac{8\pi}{\lambda}\sqrt{P_1 P_2}\sin\left(\frac{4\pi \text{OPL}}{\lambda}\right). \tag{3}$$

P_1 depends further on the incident optical power P_0 and the reflectivity of the first interface R_1 (the Fresnel reflection between the probe fiber and the air). P_2 depends on the incident optical power P_0 transmitted through R_1, the reflectivity of the second interface R_2, and the coupling coefficient $\beta(z = 2L)$ between the field back-reflected from the interface R_2 and the probe fiber fundamental mode after the propagation distance $2L$ along the propagation axis z

$$P_1 = P_0 R_1 \tag{4}$$

$$P_2 = P_0(1-R_1)^2 R_2 \beta^2(z). \tag{5}$$

By assuming a Gaussian distribution for the radial intensity distribution in the gas microcell, axially aligned fibers, and parallel interfaces, the coupling coefficient $\beta(z)$ can be estimated as [22]

$$\beta(z) = \frac{2w_0 w(z)}{w_0^2 + w(z)^2} \tag{6}$$

$$w(z) = w_0\sqrt{1+\left(\frac{z\lambda}{\pi w_0^2}\right)^2}. \tag{7}$$

In the expression above w_0 represents the mode field radius of the probe fiber, while $w(z)$ presents the Gaussian beam radius at a distance z measured from the probe fiber end. Inserting expressions (4), (5), (6), and (7) into (3) results in

$$\frac{dP_r}{d\text{OPL}} = -\frac{8\pi}{\lambda}P_0(1-R_1)\frac{\sqrt{1+\left(\frac{z\lambda}{\pi w_0^2}\right)^2}}{2+\left(\frac{z\lambda}{\pi w_0^2}\right)^2} \times \sqrt{R_1 R_2}\sin\left(\frac{4\pi \text{OPL}}{\lambda}\right). \tag{8}$$

When the wavelength of the probe laser is set to the quadrature point (QP), the sine in (8) equals ± 1, and the absolute value

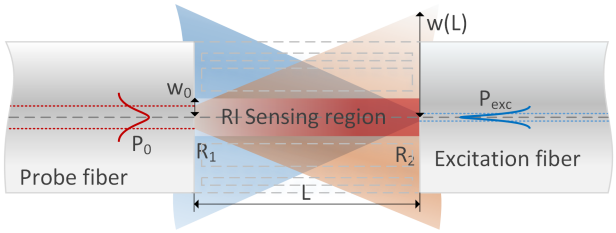

Fig. 2. Probe and excitation beam propagation within the gas cell.

of $dP_r/d\mathrm{OPL}$ can be written as

$$\frac{dP_r}{d\mathrm{OPL}} = \frac{8\pi}{\lambda_{QP}} P_0 (1-R_1) \frac{\sqrt{1+\left(\frac{z\lambda}{\pi w_0^2}\right)^2}}{2+\left(\frac{z\lambda}{\pi w_0^2}\right)^2} \sqrt{R_1 R_2}. \quad (9)$$

The OPL change caused by gas absorption of the excitation beam can be obtained from (1). Since the excitation laser beam is not collimated, the refractive index amplitude $\widehat{n}(z)$ along the propagation axis z will vary, due to the expansion of the excitation beam radius $w_{\mathrm{exc}}(z)$

$$\widehat{n}(z) = \frac{n-1}{T_0} \frac{\alpha \widehat{P}_{\mathrm{exc}} \tau_T}{\pi w_{\mathrm{exc}}(z)^2 \rho_0 C_p} \left| E_1\left(\frac{i\omega_m \tau_T}{2}\right)\right|. \quad (10)$$

The total OPL amplitude $\widehat{\mathrm{OPL}}$ in the gas microcell can be obtained by integration of the refractive index changes along the gas microcell

$$\widehat{\mathrm{OPL}} = \int_0^L \widehat{n}(z)\, dz. \quad (11)$$

It has to be noted that, by integrating over the absolute values of the exponential integral function in (10), assumes in-phase modulation at every point along the axis. This assumption is justified for short gas microcell lengths and low excitation beam divergence.

The sensing system's normalized sensitivity s, i.e., the amplitude of the back reflected probe light power $\widehat{P}_r$ over the excitation power amplitude and absorption coefficient, can be calculated by multiplying expressions (9) and (11)

$$s = \frac{\widehat{P}_r}{\alpha \widehat{P}_{\mathrm{exc}}} = \frac{dP_r}{d\mathrm{OPL}} \cdot \frac{\widehat{\mathrm{OPL}}}{\alpha \widehat{P}_{\mathrm{exc}}} \quad (12)$$

$$s = \frac{n-1}{T_0} \frac{\tau_T}{\pi \rho_0 C_p} |E_1(i\omega_m \tau_T/2)| \int_0^L \frac{1}{w_{\mathrm{exc}}(z)^2} dz \cdot \frac{8\pi}{\lambda_{QP}} P_0 (1-R_1) \frac{\sqrt{1+\left(\frac{z\lambda}{\pi w_0^2}\right)^2}}{2+\left(\frac{z\lambda}{\pi w_0^2}\right)^2} \sqrt{R_1 R_2}. \quad (13)$$

Fig. 3(a) shows a plot of $dP_r/d\mathrm{OPL}$ and $\widehat{\mathrm{OPL}}/(\alpha \widehat{P}_{\mathrm{exc}})$ as a function of the gas cell length, while Fig. 3(b) represents the product of these two terms (i.e., s). The position of the maximum in the second plot indicates the gas microcell length L, where the highest sensitivity is obtained, indicating the optimum gas microcell length. The plots in Fig. 3 were obtained for typical values of the proposed sensor system, i.e., the wavelength of the probe laser was set to 1550 nm, while the mode field radius (w_0) of the probe fiber (SMF-28e) was set to 10.2 μm. The excitation laser operation wavelength was set to 450 nm with an excitation frequency of 400 Hz, while the gas microcell cell was filled with 2% NO_2 in dry air (Cp = 1012 $\mathrm{Jkg^{-1}K^{-1}}$ n_{air} = 1.000293, ρ_0 = 1.1978 $\mathrm{kg/m^3}$, $D_T = 2.1779 \times 10^{-05}$ $\mathrm{m^2/s}$). The mode field diameter of the excitation fiber w_{exc0} is 3 μm, and the reflectivity of the interfaces R_1 and R_2 is 0.036.

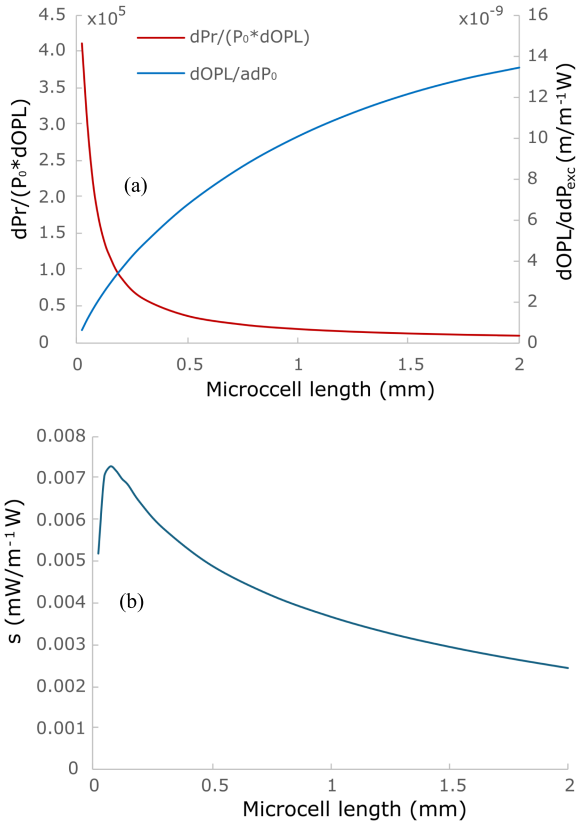

Fig. 3. (a) dPr/dOPL and $\widehat{\mathrm{OPL}}/(\alpha \widehat{P}_{\mathrm{exc}})$ at different gas microcell lengths (dPr is expressed as relative reflected optical power) and (b) product of dPr/dOPL and $\widehat{\mathrm{OPL}}/(\alpha \widehat{P}_{\mathrm{exc}})$ at different gas microcell lengths.

These results suggest an optimum gas microcell length between 150 and 200 μm for the presented setup. Preliminary experimental tests suggested that slightly longer cells yielded higher sensitivity. By manufacturing several gas microcells with different lengths, the best results were obtained with lengths around 1 mm. The most likely cause for this discrepancy between theoretical estimation and experimental observations was the difference between the expected and actual reflectance of the sensor cavities. Fabricated shorter gas microcells had lower reflectance amplitudes in the reflectance spectrum, which contrasts with results measured using reference FPI (see the Appendix). Discrepancies are thought to arise from the cell manufacturing process where multiple parameters (cleaving and splicing parameters, femtosecond laser parameters, etching parameters, and environmental parameters) affect the quality of the gas microcell resonator. The additional possible cause for discrepancies in the model and practical observations is the heat transfer between the heated gas and the optical fibers, decreasing the temperature variation in the proximity of the excitation fiber end faces. The distance in the gas over which thermal conduction will reduce the photothermal response can be estimated by the thermal diffusion length $l_T = (2D_T/w)^{1/2}$ [21], which, for the present case, was about 130 μm from each end face.

The theoretical model does not predict a limit of detection since this would require an additional investigation of noise sources of the applied laser diode, photodetectors, and

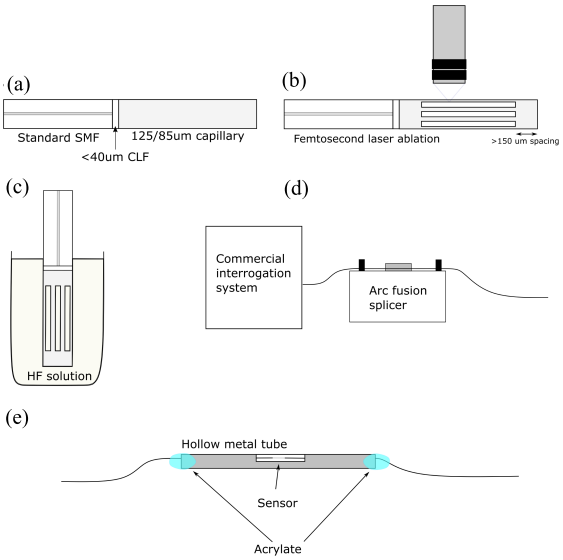

Fig. 4. Manufacturing process of the thermo-optic gas sensor: (a) splicing of a 40 μm long section of coreless fiber and 1 mm long section of the capillary to the SMF-28e probe fiber, (b) micromachining slits into the sides of the capillary, (c) etching a slit capillary to remove debris, (d) splicing an RGB-400 excitation fiber to the other side of slitted capillary, and (e) packaging the sensor into a metal holder.

transimpedance amplifiers. While care was taken to minimize all possible noise sources during system design, noise sources were not included in the theoretical model. Since preliminary tests yielded the best sensitivity using a 1 mm long gas microcell, this sensor was selected for experimental evaluation.

C. Sensor Manufacturing

The sensor structure was manufactured in several consecutive steps. First, the coreless fiber and the capillary (87 μm inner diameter) section were fusion-spliced to the probe single-mode fiber [Fig. 4(a)] using a conventional Telecom fusion splicer. The slits along the capillary were then machined via a femtosecond laser [Fig. 4(b)]. The entire structure was then immersed into a hydrofluoric (HF) solution to remove the fine debris/leftovers from machining [Fig. 4(c)]. The coreless section prevented the fiber's front surface from degrading, both during splicing, when the germanium core tends to be "pushed out" of the fiber end-face due to a viscosity mismatch between the fiber core and the cladding, and during the debris removal step using HF etching (the fiber core etches selectively faster relative to the cladding when in contact with HF [23]). In the last sensor production step, the short-cut-off wavelength single-mode lead-in fiber was spliced to the opposite side of the capillary to complete the sensor structure [Fig. 4(d)]. The produced sensor was further packaged into a metal tube with a side opening [Fig. 4(e)], to protect the sensor structure from unwanted mechanical influences, which can damage the sensor. The resulting sensing structure was solid and capable of withstanding regular handling and moderate vibrations.

III. Signal Interrogation

Relatively weak RI variations ($\Delta n < 10^{-7}$ RIU) induced by photothermal excitation of gas mixtures are at the limit

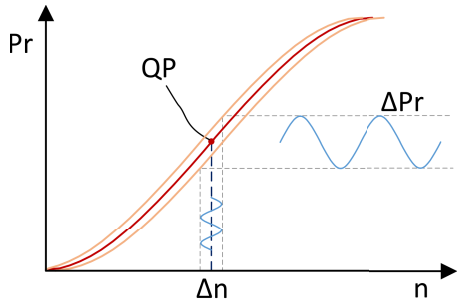

Fig. 5. Variation of reflected optical power around the QP due to variations of the refractive index.

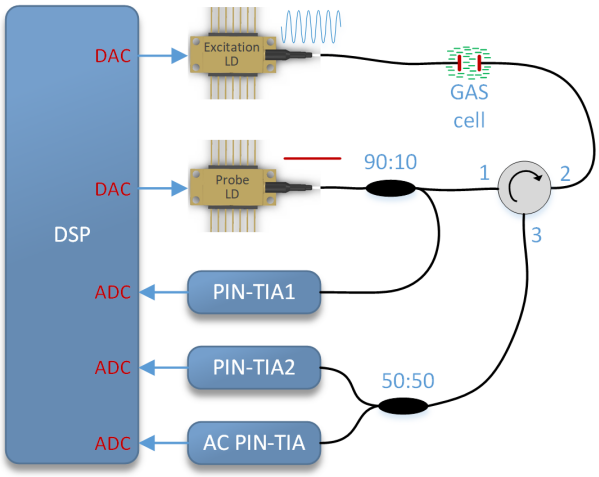

Fig. 6. Simplified schematic of the interrogation system.

of detection of established spectral interrogation methods, used for compact fiber-based FPIs [24], especially when the interrogation must be achieved dynamically at higher readout rates. Thus, alternative methods were considered, and an interrogation was applied, based on a probe laser locking onto the QP of the FPI transfer function. In this approach, the probe laser wavelength is adjusted slowly but in a way that the interfering waves' phase difference corresponds to $3\pi/2 + 2m\pi$ (m is an integer number). In this way, the probe laser is locked actively onto the QP of the FPI transfer function, while small dynamic variations of the refractive index cause variations in the FPI OPL, which, subsequently, causes variations of the light intensity reflected from the FPI (Fig. 5).

A schematic of the sensing system is presented in Fig. 6. It is based on a digital signal processing (DSP) unit that controls the probe and excitation laser diodes, an optical system that guides the probe and excitation light into the sensor, and photo-detectors that acquire optical signals.

A narrow linewidth laser diode 1550LD-6-0-0-1 (Aerodiode) that operates at 1550 nm, was selected as the probe laser source and locked onto the QP of the sensor using thermal tuning of the probe laser. Three photodetectors with a transimpedance amplifier (PIN-TIA) served to lock the probe laser, while measuring the amplitude of the reflected modulated signal simultaneously. One photodetector with a transimpedance amplifier (ac PIN-TIA) was ac coupled, and

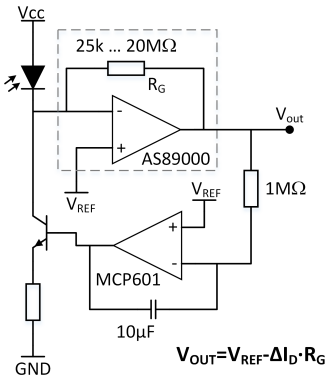

Fig. 7. Design of the transimpedance amplifier for modulated signals.

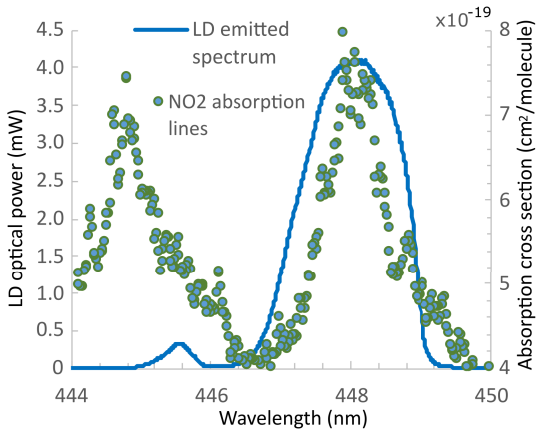

Fig. 8. Emission spectrum of the excitation laser diode compared to the absorption lines of NO_2 (HITRAN database) around 448 nm.

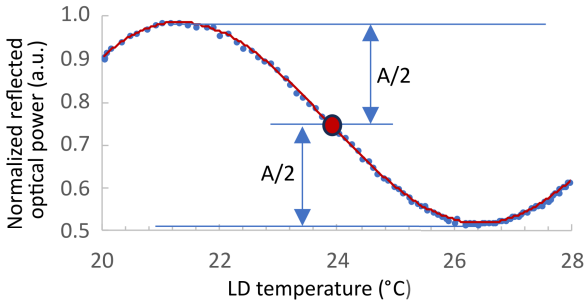

Fig. 9. Sensor's spectral characteristics acquired using thermal tuning of the probe laser diode.

designed to acquire and amplify only the modulated part of the back-reflected optical signal required for measurement of the signal amplitude. The PIN-TIA 2 acquires the total reflected optical power from the sensor, while PIN-TIA 1 acquires the probe laser diode output power, which is used to normalize the optical power acquired by PIN-TIA 2. The normalized average optical power is used as a feedback signal to maintain the probe laser diode at the QP. The amplitude of the thermo-optically modulated signal is extracted from the ac PIN-TIA using digital algorithms, and correlated to the gas concentration.

The design of the ac PIN-TIA was based on [25], where the dc current generated by the photodetector is subtracted actively by the feedback integrator, and, consequently, only the modulated part of the current generated on the photodetector is converted into voltage. Simpler ac coupling of the photodiode using a serial capacitor and a bias resistor generated significant noise, especially when high gains were applied on the transimpedance amplifier. The basic schematic of the proposed ac PIN-TIA is presented in Fig. 7, and is built around an integrated TIA AS89000 (Omron), which ensures low noise operation at high digitally programmable gains between 25 kΩ and 20 MΩ.

The modulated signal on the output of the ac PIN-TIA was further connected to the DSP's analog-to-digital converter (ADC) for digitalization and further processing.

The excitation laser diode was selected according to the target gas, i.e., its emission wavelength was matched to the selected absorption peak of the gas to be detected. Since the sensing system was characterized with NO_2, we selected a 450 nm laser diode WSLP-445-070m-4-B (Wave spectrum) with 70 mW of continuous optical power coupled into a single mode fiber RGB 400. By tuning the laser diode thermally, it was possible to align its emission wavelength to the NO_2 absorption lines at 448 nm (Fig. 8).

While the absorption of NO_2 is the highest around 405 nm, these wavelengths are not suitable for photothermal detection due to the photodissociation effect [26]. The absorption peak at 448 nm has a similar magnitude and was thus selected for demonstrating the potential of the sensing system.

Light from the excitation laser diode is guided into the sensor from the opposite side compared to the probe light. This is due mainly to the unavailability of wavelength division multiplexers (WDMs) for the selected wavelengths (1550 and 448 nm). If the probe and excitation wavelengths are compatible with WDM components, then both beams can enter the gas microcell from the same side, and the sensor could be simplified further.

A. Locking the Probe Laser Wavelength Onto the QP

Measurement initialization includes locking the probe laser wavelength onto the QP of the sensor. In the initialization step, the wavelength of the probe laser is tuned across the entire free spectral range of the FPI thermally by a built-in thermoelectric cooler (TEC) and thermistor (NTC), while the normalized reflected optical power is measured (Fig. 9). The polynomial least-square regression is then calculated for the acquired dataset, and maximum, as well as minimum normalized reflected optical powers are extracted. The normalized optical power reflected from the QP is located in the middle between the maximum and minimum reflected optical powers. After the initialization cycle, the diode is placed in a continuous output power mode of operation, while the temperature of the diode is controlled actively (by using a digital PID controller), to maintain an average back-reflected normalized light power in the middle between the minimum and the maximum of the measured power levels obtained during the initialization step.

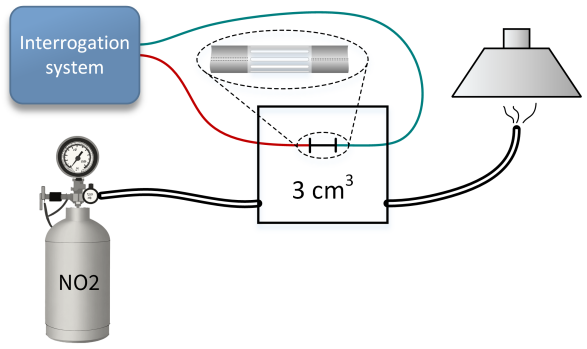

Fig. 10. Experimental setup for initial testing.

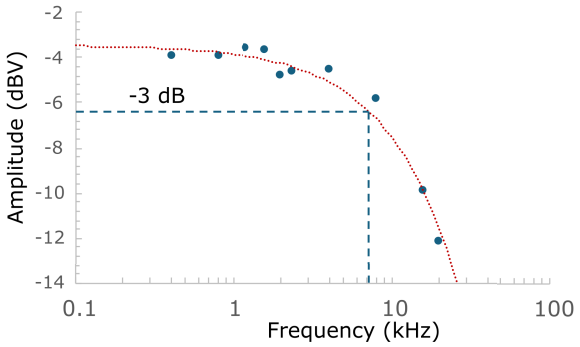

Fig. 11. Response of the sensor at different excitation frequencies.

B. Gas Sensing Algorithms

The sinusoidal modulation signal for the excitation laser diode was generated by a digital-to-analog converter (DAC) within the DSP using a look-up table. The DAC sampling clock was also shared with the ADC, to ensure synchronized probe signal generation and sampling. One period of modulation signal consisted of 50 samples stored in a lookup table of DAC. The ADC acquired 200 periods (10 000 samples) of the reflected modulated signals for a single amplitude measurement. Thus, the integration time depends on the DAC and ADC sampling clock, which is adjustable and can be calculated by multiplying the modulation frequency with 50 samples. The signal amplitude at the chosen modulation frequency was then extracted using the Goertzel algorithm [27] set to the modulation frequency. The result was further transmitted into the LabView Graphical User Interface for visualization.

IV. Experimental SetUp and Results

The sensing system was tested using two different test benches. The initial tests (Fig. 10) were performed using a 2% NO_2-air mixture. This test bench was used to investigate the sensor's dynamic properties and to estimate the system's detection limit toward longer integration times. The gas cylinder with a preprepared 2% NO_2 mixture was connected to a compact aluminum gas-tight enclosure with a volume of about 3 cm^3 through an adjustable pressure regulator, which was used to set a fixed flow rate through the gas-tight enclosure. The gas-tight enclosure included an inlet, an outlet for gas delivery, and two small holes/openings on opposite sides for the insertion of the gas microcell. All the openings were sealed using a vacuum sealant once the sensor was installed. The outlet of the gas-tight enclosure was connected to the fume hood.

We analyzed the signal amplitude and background noise level across the excitation frequency range between 50 Hz and 20 kHz (Fig. 11), to determine the optimal excitation laser modulation frequency. The power of the excitation laser diode was set to 70 mW, while the output optical power of the probe laser diode (1550 nm) was set to approximately 20 mW. The probe laser's wavelength was locked actively onto the FPI's QP by controlling the diode's temperature, as already described above. The FPI/ac PIN-TIA output signal was then amplified using a 2 MΩ feedback resistor and digitized. The digitized data frames were then subjected to a fast Fourier transformation (FTT), to obtain a distribution of frequency components within the acquired signal band (i.e., between 50 Hz and 20 KHz). The acquired spectra were further integrated continuously over 100 s intervals.

After that, the gas microcell was filled with synthetic air, to obtain background noise levels across the spectrum of interest. Some frequency components were present in the background signal [Fig. 12(b)], resulting from the limited power supply filtering. However, these frequency components did not disturb the measurement, as the excitation frequency can be chosen well clear of them.

In the next step, the gas microcell was filled with a 2% gas mixture of NO_2. The excitation frequency was then varied between 50 Hz and 20 kHz, while the signal amplitude in the time and frequency domain was observed at the ac PIN-TIA's output. The dynamic characteristics (Fig. 11) show that the bandwidth of the sensor was approximately 7 kHz. In addition, we measured the bandwidth of 600 and 350 μm long gas microcells, which exhibited similar bandwidths (600 μm gas microcell had a bandwidth of 8 kHz, and 350 μm gas microcell had a bandwidth of 8.8 kHz with uncertainty in the range of about 1 kHz).

As anticipated by 1, the amplitude of the signal is the highest at lower modulation frequencies. However, due to the probe laser's 1/f noise characteristic, the SNR can be enhanced by choosing higher excitation frequencies. Fig. 12(a) shows an example of a time domain recording of the background noise and reflected signal with 2% NO_2 present in the gas-tight enclosure and an excitation frequency of 400 Hz. Additionally, background noise and the reflected signal are presented in the frequency domain [Fig. 12(b)] for the same excitation frequency.

From the difference between the obtained signal amplitude and the background noise level, it is visible (Fig. 12) that the highest SNR was observed at frequencies around 400 Hz, where background noise flattens at about −60 dBV. This result might depend on the chosen laser diode phase and random intensity nose characteristics, selected electronics components, and FPI geometry. However, 400 Hz proved to be the optimal excitation frequency for the particular configuration, as presented here.

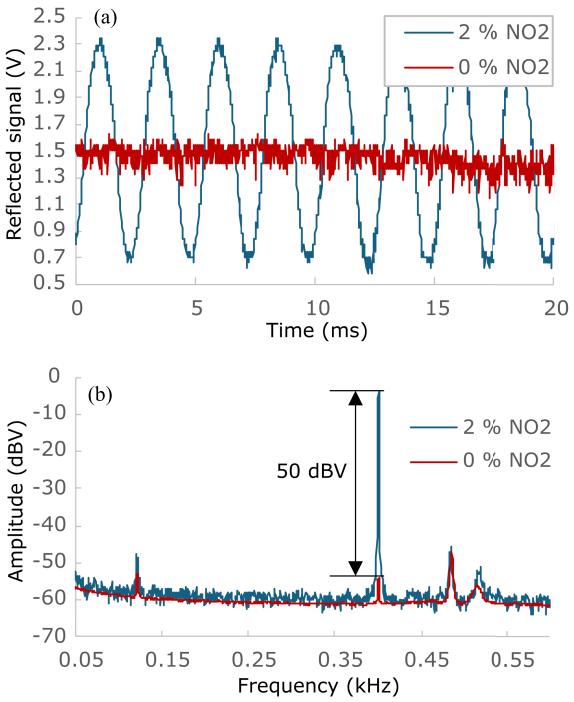

Fig. 12. (a) Amplitude of the ac PIN-TIA signal in the time domain (2% NO_2 concentration compared to dry air) and (b) FFT of the signal. The excitation frequency was set to 400 Hz.

When 400 Hz exaction was applied, replacing the synthetic air in the gas microcell with a 2% NO_2-air mixture caused an amplitude increase of about 50 dBV. This equals an SNR of about 1:316, which further corresponds to a detection limit of about 63 ppm of NO_2 in synthetic air (when using a 100 s integration time). When only synthetic air was present within the gas microcell, we observed traces of the modulation signal with an amplitude of about 5 dB. This most likely resulted from heating certain parts of the gas microcell, due to the high excitation power.

The calibration curve of the sensor was determined using a gas dilutor as shown in Fig. 13. The gas dilutor [28] was added upstream of the gas-tight enclosure, and nitrogen was used instead of synthetic air. The NO_2 gas cylinder for this experiment contained a 1000 ppm mixture of NO_2 in synthetic air. Adjusting the gas dilutor's mixing ratio provided gas concentrations from 25 up to 1000 ppm.

Before the measurement of the calibration curve, we performed a long-term measurement of the photothermal absorption signal in the nitrogen atmosphere to obtain the background noise level. The calibration curve was then obtained by increasing the gas concentrations gradually and observing the signal amplitude measured by the interrogation system. The integration time was set to 200 s, and the background amplitude was subtracted from the measurement [Fig. 14]. A linear fit applied to the measurement points showed good linearity with an R-squared value of 0.9995.

The transition from a concentration of 55 ppm of NO_2 to 100 ppm, recorded with an integration time of 10 s, is presented in Fig. 15, indicating clearly a resolution better than 20 ppm.

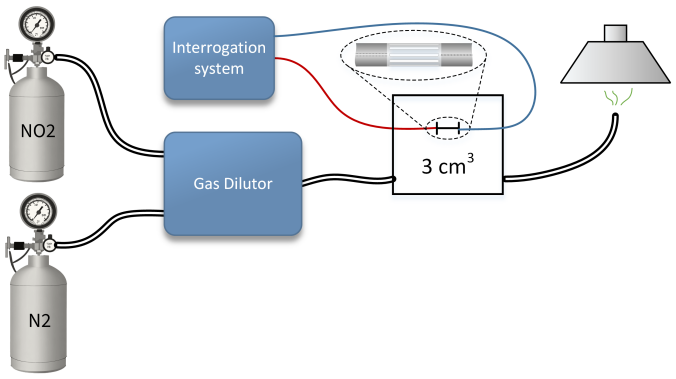

Fig. 13. Experimental setup for the measurement of static characteristics.

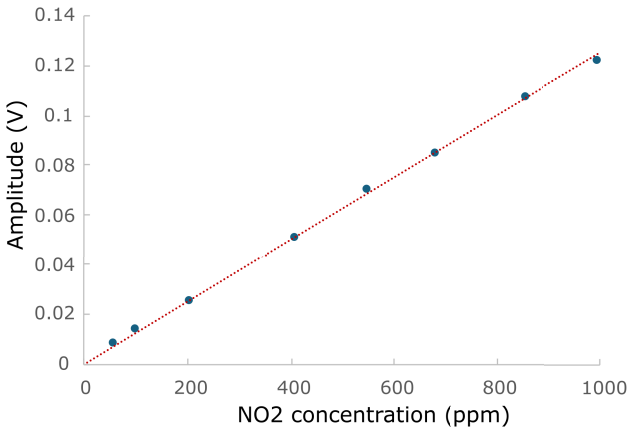

Fig. 14. Calibration curve and sensor response over time during measurement of the calibration curve. The background-corrected sensor response (blue dots) for different NO_2 concentrations with a linear fit (red dotted line), indicating the linearity of the system.

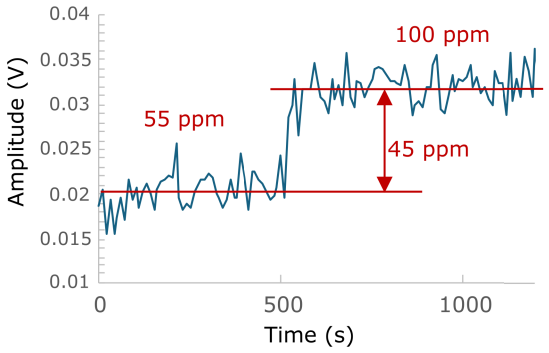

Fig. 15. Amplitude measured by the sensing system during the transition from 55 to 100 ppm of NO_2 with an integration time of 10 s.

Finally, Allan deviation measurements were performed using the background signal amplitude over a period of more than 5 h. The measurement was performed without NO_2 in the gas-tight enclosure. Also, the excitation laser was turned on during the measurement. The results are shown in Fig. 16 and indicate that the SNR can be improved by increasing the integration time up to 1000 s, which improves the 1σ detection limit below 3 ppm.

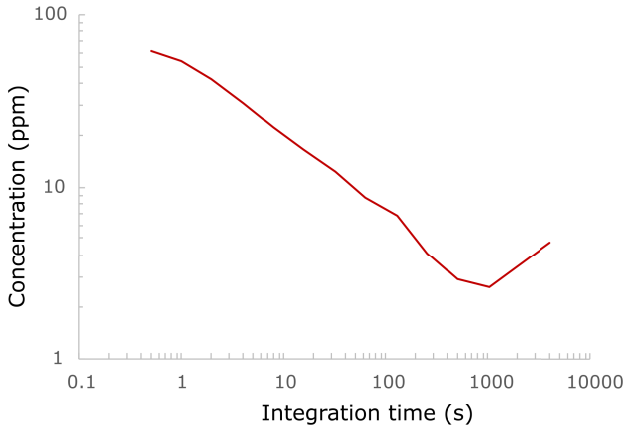

Fig. 16. Allan deviation of the measured background amplitude.

From the limit of detection at 10 s integration time (20 ppm), we estimated the normalized noise equivalent absorption (NNEA) using a corresponding average absorption coefficient of 0.3×10^{-3} cm^{-1}, 70 mW excitation power, and systems bandwidth of 0.032 Hz. NNEA in this case is 1.16×10^{-4} cm^{-1} W Hz$^{-1/2}$. Compared to other all-fiber photothermal sensing solutions that reached NNEA of 4.29×10^{-7} cm^{-1} W Hz$^{-1/2}$ (NO) [16], 2.7×10^{-7} cm^{-1} W Hz$^{-1/2}$ (Acetylene) [19], and 7.5×10^{-9} cm^{-1} W Hz$^{-1/2}$ (CH_4) [10], the presented solution exhibits higher NNEA. However, it is necessary to stress that the proposed sensor is very short (1 mm) compared to other all-fiber solutions and is compatible with a broad range of excitation and probe wavelengths (bringing excitation and probe light from opposite directions removes the need for dual wavelength compatible optical components, which might be inaccessible or hard to design). Lastly, the open cell design enables unobstructed gas exchange, which significantly decrease the response time of the proposed gas cell (most all fiber solutions with high NNEA utilizes PCF/HC fibers of substantial lengths, with small side holes which limits gas exchange dynamics).

V. Conclusion

We demonstrated the design and performance of a compact, all-fiber, all-silica, low-finesse Fabry–Perot gas sensor utilizing photothermal spectroscopy. A compact and cost-efficient interrogation system based on QP-locking and lock-in detection techniques was realized using only broadly available optoelectronic components. The sensor was composed of a short (1 mm) glass capillary with integrated multiple side slits, which were fusion-spliced in between two fibers that each delivered probe or excitation laser light into the sensing region. Operation of the system was demonstrated by NO_2 detection in air/nitrogen, where the achieved limit of detection was in the range of 20 ppm using an integration time of 10 s, and 3 ppm with an integration time of 1000 s. The presented sensing system shows promising potential for different practical field applications due to its compact design (portable) and cost-efficient fabrication.

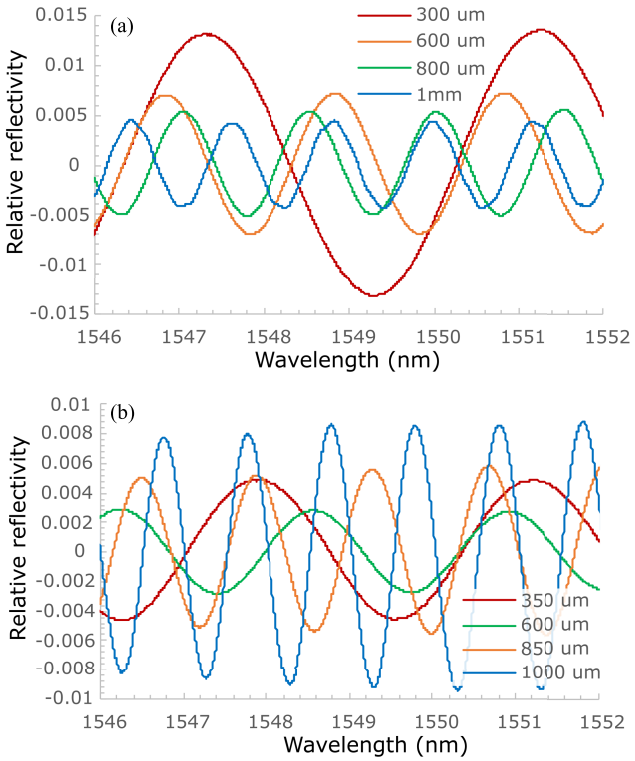

Fig. 17. Relative reflectance spectrums of (a) reference FPIs and (b) gas microcells of similar lengths.

TABLE I
Comparison of Reference FPIs and Gas Microcells

	300 µm	600 µm	800 µm	1 mm
Reference FPI amplitude	0.026	0.0135	0.0094	0.008
Gas microcell amplitude	0.00933	0.0057	0.01	**0.017**

Appendix

To find the possible reasons for the lower sensitivity of shorter gas cells, we performed reflectance amplitude measurements of reference interferometers of various lengths and compared them to fabricated gas microcells of the same lengths. Reference interferometers were created by aligning flat cleaved optical fibers at defined lengths. Reflectance spectrums were acquired using the spectral optical interrogation system NI PXIe-4844 (National instruments), and the bias component was removed for easier comparison. Reflectance spectrums are presented in Fig. 17(a) for reference interferometers and Fig. 17(b) for gas microcells of similar lengths.

Measured amplitudes of relative reflectance are presented in Table I which shows that 300 and 600 μm gas microcells yielded significantly lower amplitude of reflectance spectrums compared to reference FPI, while a 1 mm long gas microcell yielded the highest amplitude.

References

[1] J. Shao et al., "Multigas detection using a sample-grating distributed Bragg reflector diode laser," *Appl. Opt.*, vol. 52, no. 31, pp. 7462–7468, Nov. 2013, doi: 10.1364/ao.52.007462.

[2] M. Njegovec and D. Donlagic, "A fiber-optic gas sensor and method for the measurement of refractive index dispersion in NIR," *Sensors*, vol. 20, no. 13, p. 3717, Jul. 2020, doi: 10.3390/s20133717.
[3] F. Xu, Z. Lv, X. Lou, Y. Zhang, and Z. Zhang, "Nitrogen dioxide monitoring using a blue LED," *Appl. Opt.*, vol. 47, no. 29, pp. 5337–5340, Oct. 10, 2008, doi: 10.1364/ao.47.005337.
[4] S. Bi, S. Qian, C. Tian, Q. Zhang, Y. Yu, and Z. Wang, "Trace gas detection system based on photoacoustic and photothermal spectroscopy using ring fiber laser and quartz tuning fork," *IEEE Sensors J.*, vol. 23, no. 9, pp. 9229–9236, May 2023, doi: 10.1109/JSEN.2023.3244027.
[5] K. Krzempek, "A review of photothermal detection techniques for gas sensing applications," *Appl. Sci.*, vol. 9, no. 14, p. 2826, Jul. 2019, doi: 10.3390/app9142826.
[6] W. Jin, Y. Cao, F. Yang, and H. L. Ho, "Ultra-sensitive all-fibre photothermal spectroscopy with large dynamic range," *Nature Commun.*, vol. 6, no. 1, p. 6767, Apr. 2015, doi: 10.1038/ncomms7767.
[7] P. Breitegger, B. Lang, and A. Bergmann, "Intensity modulated photothermal measurements of NO2 with a compact fiber-coupled Fabry–Pérot interferometer," *Sensors*, vol. 19, no. 15, p. 3341, Jul. 2019, doi: 10.3390/s19153341.
[8] J. Waclawek, V. Bauer, H. Moser, and B. Lendl, "2F-wavelength modulation Fabry–Perot photothermal interferometry," *Opt. Exp.*, vol. 24, no. 25, pp. 28959–28968, Dec. 2016. [Online]. Available: https://opg.optica.org/oe/fulltext.cfm?uri=oe-24-25-28958&id=355845, doi: 10.1364/OE.24.028958.
[9] Y. Tan, W. Jin, F. Yang, Y. Jiang, and H. L. Ho, "Cavity-enhanced photothermal gas detection with a hollow fiber Fabry–Perot absorption cell," *J. Lightw. Technol.*, vol. 37, no. 17, pp. 4222–4228, Sep. 2019, doi: 10.1109/JLT.2019.2922001.
[10] C. Yao, S. Jiang, S. Gao, Y. Wang, W. Jin, and W. Ren, "Photothermal gas detection with a dithered low-finesse fiber-optic Fabry-Pérot interferometer," *J. Lightw. Technol.*, vol. 41, no. 2, pp. 745–751, Jan. 15, 2023, doi: 10.1109/jlt.2022.3215807.
[11] Z. Yang, G. Yin, C. Liang, and T. Zhu, "Photothermal interferometry gas sensor based on the first harmonic signal," *IEEE Photon. J.*, vol. 10, no. 2, pp. 1–7, Apr. 2018, doi: 10.1109/JPHOT.2018.2821845.
[12] J. P. Waclawek, C. Kristament, H. Moser, and B. Lendl, "Balanced-detection interferometric cavity-assisted photothermal spectroscopy," *Opt. Exp.*, vol. 27, no. 9, pp. 12183–12195, Apr. 29, 2019, doi: 10.1364/oe.27.012183.
[13] U. Radeschnig, A. Bergmann, and B. Lang, "Optimization of the optical path length amplitude for interferometric photothermal gas and aerosol sensing considering advection: A theoretical study," *J. Appl. Phys.*, vol. 135, no. 9, Mar. 2024, Art. no. 094501, doi: 10.1063/5.0184357.
[14] B. Visser et al., "Waveguide based passively demodulated photothermal interferometer for light absorption measurements of trace substances," *Appl. Opt.*, vol. 62, no. 2, pp. 374–384, Jan. 2023, doi: 10.1364/ao.476868.
[15] F. Yang, W. Jin, Y. Lin, C. Wang, H. Lut, and Y. Tan, "Hollow-core microstructured optical fiber gas sensors," *J. Lightw. Technol.*, vol. 35, no. 16, pp. 3413–3424, Aug. 15, 2017, doi: 10.1109/JLT.2016.2628092.
[16] K. Krzempek, P. Jaworski, P. Kozioi, and W. Belardi, "Antiresonant hollow core fiber-assisted photothermal spectroscopy of nitric oxide at 5.26 μm with parts-per-billion sensitivity," *Sens. Actuators B, Chem.*, vol. 345, Oct. 2021, Art. no. 130374, doi: 10.1016/j.snb.2021.130374.
[17] S. Liu et al., "Antiresonant hollow-core fiber assisted photothermal spectroscopy for the detection of ammonia in human breath," *Opt. Fiber Technol.*, vol. 72, Sep. 2022, Art. no. 102987, doi: 10.1016/j.yofte.2022.102987.
[18] H. Bao et al., "Modeling and performance evaluation of in-line Fabry–Perot photothermal gas sensors with hollow-core optical fibers," *Opt. Exp.*, vol. 28, no. 4, pp. 5423–5435, Feb. 2020, doi: 10.1364/oe.385670.
[19] F. Yang, Y. Tan, W. Jin, Y. Lin, Y. Qi, and H. L. Ho, "Hollow-core fiber Fabry–Perot photothermal gas sensor," *Opt. Lett.*, vol. 41, no. 13, pp. 3025–3028, Jul. 2016, doi: 10.1364/ol.41.003025.
[20] Y. Hong et al., "Oxygen gas sensing with photothermal spectroscopy in a hollow-core negative curvature fiber," *Sensors*, vol. 20, no. 21, p. 6084, Oct. 2020, doi: 10.3390/s20216084.
[21] S. Bialkowski, N. G. C. Astrath, and M. Proskurnin, *Photothermal Spectroscopy Methods*, 2nd ed. Hoboken, NJ, USA: Wiley, 2019.
[22] W. Joyce and B. Deloach, "Alignment of Gaussian beams," *Appl. Opt.*, vol. 23, no. 23, pp. 4187–4196, 1984, doi: 10.1364/AO.23.004187.
[23] E. Cibula and D. Donlagic, "Low-loss semi-reflective in-fiber mirrors," *Opt. Exp.*, vol. 18, no. 11, pp. 12017–12026, 2010.
[24] R. Pan et al., "All-fiber Fabry–Perot interferometer gas refractive index sensor based on hole-assisted one-core fiber and Vernier effect," *IEEE Sensors J.*, vol. 21, no. 14, pp. 15417–15424, Jul. 15, 2021, doi: 10.1109/JSEN.2021.3075867.
[25] T. Instruments, "AC-coupled transimpedance amplifier circuit," Analog Engineer's Circuit, Texas Instrum., Dallas, TX, USA, Appl. Note.
[26] J. G. Calvert, S. Madronich, E. P. Gardner, J. A. Davidson, C. A. Cantrell, and R. E. Shetter, "Mechanism of nitrogen dioxide photodissociation in the energy-deficient region at 404.7 nm," *J. Phys. Chem.*, vol. 91, no. 25, pp. 6339–6341, Dec. 1987, doi: 10.1021/j100309a006.
[27] G. Goertzel, "An algorithm for the evaluation of finite trigonometric series," *Amer. Math. Month.*, vol. 65, no. 1, pp. 34–35, Jan. 1958, doi: 10.2307/2310304.
[28] P. Breitegger and A. Bergmann, "A precise gas dilutor based on binary weighted critical flows to create NO_2 concentrations," in *Proc. MDPI*, 2018, vol. 2, no. 13, p. 998.

Matej Njegovec received the B.S. degree and the Ph.D. degree in electrical engineering from the University of Maribor, Maribor, Slovenia, in 2008 and 2013, respectively.

He is an Assistant Professor at the University of Maribor. His main research interests include fiber optic sensors, optical sensor interrogation techniques, and the design of optoelectronic systems. He has an excellent background in analog and RF circuit design, semiconductor light sources, optoelectronic components, modulation techniques, signal processing of modulated light signals, and general signal integration techniques related to optical sensors. His biggest motive is to find innovative and cost-efficient solutions for fiber-optic sensors that would allow for the introduction of fiber-sensor technology into a broader range of practical applications.

Jure Javornik received the bachelor's and master's degrees in electrical engineering from FERI UM, Maribor, Slovenia, in 2019 and 2022, respectively, where he is currently pursuing the Ph.D. degree.

During the master's degree, he was working on femtosecond laser machining procedures for fiber-optic sensor fabrication. Upon the degree completion, he started working as a Junior Researcher at the Laboratory for Electrooptical and Sensor Systems (LEOSS), stationed at FERI UM. His field of research includes femtosecond laser micromachining, selective etching, type 2 FBG inscription, fiber-optic sensor design, fabrication, and cost-efficient interrogation techniques.

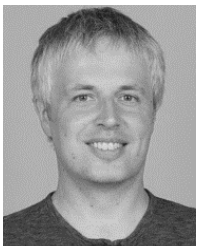

Simon Pevec received the Ph.D. degree in electrical engineering from the University of Maribor, Maribor, Slovenia, in 2014.

He is an Assistant Professor at the University of Maribor. He has more than 15 years of research experience in the field of photonics, optoelectronics, MOEMS, sensors, and measurements. His greatest experiences are related to fiber-based Fabry–Perot sensors, multiparameter sensors, optoelectronics system design, and micromachining of optical fibers including selective etching; all to produce and develop all kinds of miniature all-fiber Fabry–Perot sensors and sensors systems.

Vedran Budinski received the B.Sc. and Ph.D. degrees from the Faculty of Electrical Engineering and Computer Science, University of Maribor, Maribor, Slovenia, in 2012, and 2017, respectively.

Since 2012, he has been working as a Researcher at the Laboratory for Electro-Optical and Sensor Systems, University of Maribor. His research interests include fiber optic sensors for measuring twist/rotation, fiber optic microfluidic sensors, the design of miniature microstructures on the tip of an optical fiber, and employing various micromachining techniques for detecting various physical and chemical parameters.

Tomaz Gregorec, photograph and biography not available at the time of publication.

Benjamin Lang received the master's and Ph.D. degrees in technical physics from the Faculty of Electrical and Information Engineering, Graz University of Technology, Graz, Austria, in 2015 and 2020, respectively.

He is a University Assistant at the Institute for Electrical Measurement and Sensor Systems, Graz University of Technology. He is interested in researching laser-based optical sensing techniques, focusing on laser absorption spectroscopy (tunable diode, photoacoustic, photothermal) in gases and condensed phases.

Manuel Tanzer received the master's degree in technical physics and the degree in physical energy and measurement engineering from the Technical University of Technology, Vienna, Austria. He is pursuing the Ph.D. degree with the Institute of Electrical Measurement and Sensor Systems, Graz University of Technology, Graz, Austria.

His research topic is the miniaturization of photothermal gas and aerosol sensors.

Alexander Bergmann is a Professor of Electronic Sensor Systems and the Head of the Institute of Electrical Measurement and Sensor Systems, Graz University of Technology, Graz, Austria, where he is also the Laboratory Head of the Christian Doppler Laboratory for Structured Matter-Based Sensing, where he and his team investigate highly sensitive sensing structures based on structured light and matter. His research is dedicated to sensor effects, sensor materials, and sensor systems. One focus area is the quantification of fluid as well as aerosol properties (air polluters and climate forcers) with an emphasis on high temporal resolution.

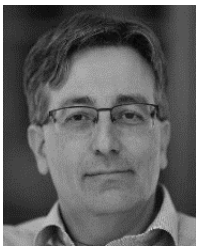

Denis Đonlagić (Member, IEEE) received the first Ph.D. degree from the University of Ljubljana, Ljubljana, Slovenia, in 1998, and the second Ph.D. degree from the University of Strathclyde, Glasgow, U.K., in 2000.

He is a Full Professor at the University of Maribor, Maribor, Slovenia. He has a broad background in the fields of photonics systems, opto-electronics systems, optical fibers, and MOEMS. In particular, he has research and development experience in the fields of optical fiber sensors, optical fibers, and opto-electronics system design. His focus is in finding new scientific paradigms and technology concepts, while bringing them into practical applications.

Dr. Đonlagić is a member of the Editorial Board of the *Journal of Lightwave Technology*.